

Effects of Temperature, Salinity, and Fluid Type on Acoustic Characteristics of Turbulent Flow Around Circular Cylinder

Sertaç Bulut¹ · Selma Ergin¹

Received: 29 December 2019 / Accepted: 22 September 2020 / Published online: 11 May 2021
© Harbin Engineering University and Springer-Verlag GmbH Germany, part of Springer Nature 2021

Abstract

The effects of the temperature, salinity, and fluid type on the acoustic characteristics of turbulent flow around a circular cylinder were numerically investigated for the Reynolds numbers of 2.25×10^4 , 4.5×10^4 , and 9.0×10^4 . Various hybrid methods—Reynolds-averaged Navier–Stokes (RANS) with the Ffowcs Williams and Hawkings (FWH) model, detached-eddy simulation (DES) with FWH, and large-eddy simulation with FWH—were used for the acoustic analyses, and their performances were evaluated by comparing the predicted results with the experimental data. The DES-FWH hybrid method was found to be suitable for the aero- and hydro-acoustic analysis. The hydro-acoustic measurements were performed in a silent circulation channel for the Reynolds number of 2.25×10^4 . The results showed that the fluid temperature caused an increase in the overall sound pressure levels (OASPLs) and the maximum sound pressure levels (SPL_T) for the air medium; however, it caused a decrease for the water medium. The salinity had smaller effects on the OASPL and SPL_T compared to the temperature. Moreover, the main peak frequency increased with the air temperature but decreased with the water temperature, and it was nearly constant with the change in the salinity ratio. The SPL_T and OASPL for the water medium were quite higher than those for the air medium.

Keywords Hydro- and aero-acoustics · Computational acoustics · Acoustic measurement · Flow noise · Hybrid acoustic methods · Temperature effect · Salinity effect

1 Introduction

The requirements for reduced noise levels in engineering applications have become increasingly demanding, with great limitations on aero- and hydro-systems. Health and comfort problems, environmental noise pollution, and the negative impacts on marine mammals are some of the critical issues resulting from high

noise levels. A further understanding of the nature and origins of acoustic phenomena is necessary to propose applicable solutions for reducing and controlling the noise levels.

The investigation of the fluid properties affecting the acoustic characteristics has great importance for aero- and hydro-acoustics, due to the wide range of applications in many engineering fields. Particularly, the seawater properties have a crucial impact on underwater acoustic communication systems (Zaibi et al. 2009). These systems are commonly used in many open-sea applications for offshore exploration, pollution monitoring, surveillance systems, oceanographic research, assisted navigation, military purposes, and mining prospecting. Unmanned underwater vehicles are also equipped with underwater acoustic sensors (Akyildiz et al. 2005; Imran et al. 2017; Sendra et al. 2016). The physical characteristics of ocean and seawater such as temperature and salinity significantly affect the underwater wireless communication network and acoustic signal characteristics (Awan et al. 2019). The temperature and salinity of water have various effects on the properties of the acoustic communication channels (Sehgal et al. 2009). It is necessary to understand the effects of these properties to obtain optimal capacity and efficiency. Furthermore, the air temperature significantly affects the

Article Highlights

- A numerical investigation on the effects of the temperature, salinity, and fluid type on the hydro- and aero- acoustic characteristics of turbulent flow around a circular cylinder was performed.
- The hydro-acoustic measurements were carried out in a circulation channel.
- The performances of different hybrid methods were evaluated by comparing the predicted results with the experimental data.
- The values of main acoustic characteristics were increased by temperature for the air medium, but decreased for the water medium.

✉ Selma Ergin
ergin@itu.edu.tr

¹ Department of Naval Architecture and Marine Engineering, Istanbul Technical University, 34469 Istanbul, Turkey

aerodynamic and aero-acoustic fields of turbulent jets. Jet noise has become one of the most important fields of research due to its effects on aircraft overall noise characteristics. However, it is quite a challenging problem in aero-acoustics because of the insufficient understanding of noise generation mechanisms. Some studies (e.g., Tanna et al. 1975; Bodony and Lele 2005; Bridges 2006; Bogey and Marsden 2013; Benderskiy and Lyubimov 2014; Kuo et al. 2015) have been performed to evaluate the effects of the fluid temperature on the aerodynamic and acoustic fields of turbulent jets. This paper presents a comprehensive investigation of the effects of temperature, salinity, and fluid type on the aero- and hydro-acoustic characteristics of turbulent flow around a circular cylinder. The study provides a new perspective on the understanding of the phenomena for the concerned application areas.

The flow noise around a cylinder is an important problem to understand the mechanisms of dynamic noise, as it consists of the fluid forces, pressure distribution, wake interference, flow separation, and turbulence characteristics. It occurs in a wide variety of engineering applications, including civil engineering (cables in bridges, fences, and transmission lines), transportation system engineering (aircraft landing gears and train pantograph), and marine engineering (risers, pipelines, and the hard tank of the offshore platforms). However, the noise produced by a viscous flow over a cylinder is difficult to calculate at moderate and high Reynolds numbers because of its extremely complicated structure. Flow separation as a result of adverse pressure gradient and the shedding of vortices through the interaction between both separated shear layers are some of the important aspects concerning the flow field around a cylinder. In addition, the computation of the flow noise has several challenges due to the complex physics of noise production and propagation and the presence of multiple sources, dispersion, and dissipation. There is a large disparity in energy and length scales between the acoustic and flow fields. Large distances are necessary to examine the acoustic wave propagation. Both aspects make unfeasible the direct solution of the Navier–Stokes equations (direct numerical simulation) for computational acoustics, except for limited applications such as 2-D cases or elementary configurations (for example, see Ianniello and De Bernardis 2015; Mahato et al. 2018; Dawi and Akkermans 2018; Ganta et al. 2019). Hybrid methods, which allow separating the fluid dynamic problem from the acoustic one, are regarded as an alternative. The flow field can be simulated by employing a turbulence model, while the acoustic solver can use any of the acoustic analogies. The first comprehensive study in the computational acoustic field was known as the Lighthill analogy. The main idea of this analogy was that the fundamental conservation laws of mass and momentum were rearranged into an inhomogeneous wave equation (Lighthill 1952). Proudman (1952) derived approximate analytical formulas based on the Lighthill analogy for the estimation of acoustic

sound intensity. Curle (1955) extended the analogy for the presence of a stationary body in the flow field. Subsequently, Williams and Hawkings (1969) derived a more comprehensive formulation by considering the body in motion. For the acoustic analysis of the fluid-body interactions, this formulation provides a physically consistent wave-propagation model. Brentner and Farassat (2003) evaluated the Ffowcs Williams and Hawkings (FWH) equation for the modeling of aerodynamically generated sound of rotors by comparing the Kirchhoff formulation. Farassat's formulations 1 and 1A were developed as an efficient way to solve the FWH equation with the surface sources when objects move at subsonic speeds (Farassat and Succi 1983; Farassat 2007). The hydrodynamics and noise behavior of marine propellers have been investigated through FWH equations under various operational conditions (Ianniello and De Bernardis 2015; Ianniello 2016; Bagheri et al. 2017; Testa et al. 2018). By employing a noise prediction code based on formulation 1A, Cox et al. (1997) examined the sound pressure levels (SPLs) generated by the flow over a circular cylinder. Choi et al. (2016) performed acoustic analysis to estimate the turbulence-induced noise of a submerged cylinder by comparing the FWH method without quadrupole sources and the permeable FWH method with quadrupole sources. Cianferra et al. (2018) analyzed the hydro-acoustic fields of three elementary geometries (sphere, cube, and prolate spheroid) through numerical simulations coupling large-eddy simulation (LES) and FWH. Cianferra et al. (2019) assessed the accuracies of the different numerical methodologies to solve the FWH equation and predict the noise generated by a finite-size square cylinder immersed in uniform flow. Zhang et al. (2019) evaluated the noise from the flow around a circular cylinder by using LES and FWH on solid and porous surfaces.

There is limited experimental research on the hydro-acoustic characteristics of submerged bodies. In contrast, aero-acoustic measurements have been adequately performed in the literature. For example, Revell et al. (1978) conducted aero-acoustic measurements on a cylinder to determine the relationship between Mach number, Reynolds number, and SPLs. Lockard et al. (2007) experimentally investigated the radiated noise by tandem cylinders in air medium and concluded that the downstream cylinder dominated the noise radiation. Hutcheson and Brooks (2012) performed aero-acoustic experiments to examine the effect of Reynolds number, surface roughness, freestream turbulence, proximity, and wake interference on the radiated noise for single and multiple rod configurations. Liu et al. (2011) conducted experimental research on the underwater radiated noise of a submarine by evaluating the double-peak phenomenon. Bosschers et al. (2013) experimentally investigated the noise levels of the towing carriage in the depressurized wave basin. A silent towing carriage has been developed for measuring surface ship flow noise. Choi et al. (2017) developed the formulation

Q1As considering quadrupole sources and performed hydro-acoustic measurements to estimate noise levels around a submerged cylinder.

Bulut and Ergin (2018) performed a numerical investigation on the acoustic characteristics of the circular cylinder. The study was based on the low-precision Reynolds-averaged Navier–Stokes (RANS) model and k- ω with FWH in the simulations. The study extended the previous work of Bulut and Ergin (2018) by expanding the temperature and salinity ranges, presenting new hydro-acoustic experimental data, and using more sophisticated turbulence modeling techniques: detached-eddy simulation (DES) and LES. Furthermore, the studies on the effects of temperature on acoustic characteristics remain restricted to the aero-acoustic field, especially jet noise. Studies on the effects of temperature and salinity on hydro-acoustic characteristics are lacking. Also, there is a lack of comparative evaluation of acoustic characteristics for water and air, which are the most commonly used media in which a wide range of sensitive systems operate.

The current study aims to comprehensively investigate the effects of the temperature, salinity, and fluid type on the aero- and hydro-acoustic characteristics. The ranges of temperature and salinity ratios are determined by considering the properties of the oceans and seas and their usage in engineering applications. The effects of the temperature on the acoustic properties were examined within the range of 10°C to 50°C for water and air. The effects of the salinity contributions between 10-g salt per kilogram of seawater (g/kg) and 70-g salt per kilogram of seawater (g/kg) were evaluated for water. In addition, the acoustic characteristics obtained by water and air media were compared on the frequency spectrum. Various hybrid models were reviewed in terms of their performance on the predictions of turbulent flow and acoustic characteristics. The results of hybrid methods (RANS with FWH, DES with FWH, and LES with FWH) were compared with the experimental data from the literature and this study. Considering the simulation cost of result accuracy, the hybrid method DES-FWH was chosen as an appropriate method for the analyses.

The results show that the effects of the temperature increase on the acoustic characteristics are completely different for air and water media. The main peak frequency, f_T , shifted to a lower value with an increase in the air temperature, while it increased with an increase in the water temperature. Interestingly, the main peak frequency was nearly independent of the salinity ratio. The main characteristics of the overall sound pressure level (OASPL) and the maximum SPL_T increased with the air temperature but decreased with the increase in the water temperature. The increase in these characteristics with the salinity was relatively small. The shape of the acoustic spectrum significantly changed with the fluid type. The main peak frequency within the air medium was higher than that within the water medium. The SPL_T and OASPL

values for water and air media at the same Reynolds numbers were found to be quite different.

2 Theoretical Background for Flow and Acoustic Analyses

2.1 Turbulence Modeling

The RANS, DES, and LES models were used for the modeling of flow structures and turbulence distribution in this study. The RANS models include the realizable two-layer k- ϵ model (Jones and Launder 1972) and the shear stress transport (SST) k- ω model (Menter 1993). The DES variant of the improved delayed DES (IDDES), which combines the SST k- ω model in boundary layers with LES in unsteady separated regions and the LES model, which uses the dynamic Smagorinsky subgrid-scale model to simulate small-scale motions, is chosen for the flow analyses.

Reynolds averaging and filtering processes are two common ways to turn the Navier–Stokes equations into a resolvable form so that the direct simulation of the small-scale turbulent structures can be avoided. Reynolds averaging is defined as the decomposition of any of the flow variables into a mean value $\bar{\theta}(x, t)$ and a fluctuating value $\theta'(x, t)$:

$$\theta(x, t) = \bar{\theta}(x, t) + \theta'(x, t) \quad (1)$$

The RANS equations derived from incompressible Navier–Stokes equations are presented in Eq. (2):

$$\frac{\partial}{\partial t}(\rho \bar{u}_i) + \frac{\partial}{\partial x_j}(\rho \bar{u}_i \bar{u}_j) = -\frac{\partial \bar{p}}{\partial x_i} + \frac{\partial}{\partial x_j} \left[\mu \left(\frac{\partial \bar{u}_i}{\partial x_j} + \frac{\partial \bar{u}_j}{\partial x_i} \right) \right] + \frac{\partial R_{ij}}{\partial x_j} \quad (2)$$

where \bar{u}_i and \bar{u}_j denote Reynolds-averaged velocities and \bar{p} represents the Reynolds-averaged pressure. The difference between Navier–Stokes and RANS equations is an additional term called the Reynolds stress tensor, R_{ij} , and it is defined by the Boussinesq hypothesis (Boussinesq 1877) as follows.

$$R_{ij} = -\rho \bar{u}_i \bar{u}_j = \mu_t \left(\frac{\partial \bar{u}_i}{\partial x_j} + \frac{\partial \bar{u}_j}{\partial x_i} \right) - \frac{2}{3} k \delta_{ij} \quad (3)$$

The RANS models of k- ϵ and k- ω turbulence models based on the Boussinesq hypothesis determine the eddy (turbulent) viscosity, μ_t , differently. The k- ϵ model uses the turbulent kinetic energy k and the turbulent dissipation rate ϵ to determine the eddy viscosity, while k- ω considers the turbulent kinetic energy k and the specific dissipation rate ω . The realizable two-layer k- ϵ model combines the realizable k- ϵ model with the two-layer approach. In the two-layer

approach, turbulent kinetic energy k is solved across the entire flow domain, while the turbulent dissipation rate ε and eddy (turbulent) viscosity μ_t are defined as functions of the wall distance in the layer next to the wall. The procedure of the realizable k-epsilon model allows defining certain mathematical constraints on the normal stresses in accordance with the physics of turbulence (realizability). The SST k-omega model is a two-equation model; it includes a blending function combining a k-omega model near the wall with a k-epsilon model in the far field. The model also has a new definition of eddy viscosity, which considers the effect of the transport of the principal turbulent shear stress.

LES is a transient technique in which the large-scale motions (large eddies) of turbulent flow are directly resolved, and only small-scale (subgrid scale) eddies are modeled. Spatial filtering is used to obtain the equations solved for LES, while an averaging process is utilized for RANS models. In the filtering process, each instantaneous component φ is split into a resolved (filtered) value $\widehat{\varphi}$ and a subgrid (subfiltered) value φ'' :

$$\varphi = \widehat{\varphi} + \varphi'' \quad (4)$$

The filtered equation of LES for incompressible Navier-Stokes equations is as follows:

$$\frac{\partial}{\partial t}(\rho u_i) + \frac{\partial}{\partial x_j}(\rho u_i u_j) = -\frac{\partial p}{\partial x_i} + \frac{\partial}{\partial x_i} \left[\mu \left(\frac{\partial u_i}{\partial x_j} + \frac{\partial u_j}{\partial x_i} \right) \right] - \frac{\partial R_{ij}^{\text{sgs}}}{\partial x_j} \quad (5)$$

where \widehat{u}_i and \widehat{u}_j are defined as the filtered velocities; \widehat{p} denotes the filtered pressure; and R_{ij}^{sgs} is the subgrid-scale Reynolds stress, which represents the unresolved scales. The dynamic Smagorinsky subgrid-scale model dynamically calculates the model coefficient, C_s , instead of using a single user-defined model coefficient (Germano et al. 1991; Lilly 1992). The subgrid-scale Reynolds stress for the dynamic Smagorinsky subgrid-scale model is defined as follows:

$$R_{ij}^{\text{sgs}} = -\rho \left(u_i'' u_j'' + u_i'' u_j'' + u_i'' u_j'' + u_i u_j - u_i u_j \right) \quad (6)$$

The DES is a hybrid approach that employs unsteady RANS models in near-wall regions and the LES model in regions away from the near-wall (Spalart et al. 1997). The IDDES variant of the DES makes it possible for RANS to be used in a much thinner near-wall field and presents wall-modeled LES capabilities. The applied RANS and LES length scales are combined with blending functions. The characteristic length scale of the wall-modeled LES branch of IDDES (l_{DDES}) is described as follows:

$$l_{\text{DDES}} = f_d(1 + f_e)l_{\text{RANS}} + (1 - f_d)l_{\text{LES}} \quad (7)$$

where f_e is the elevating function and \widetilde{f}_d is the empirical blending function. The turbulence length scales of the RANS and LES parts are represented as l_{RANS} and l_{LES} , respectively.

2.2 FWH Model

The FWH model is an extended formulation of the works by Lighthill (1952) and Curle (1955) for dynamic sound generated by a surface in arbitrary motion. The FWH equation is an inhomogeneous wave equation that is obtained by rearranging the continuity and the momentum equations and that can predict the far-field noise due to near-field flow (FWH 1969). The FWH equation considers all components of noise sources such as monopole $p'_T(x, t)$, dipole $p'_L(x, t)$, and quadrupole $p'_Q(x, t)$ as follows:

$$p'(x, t) = p'_T(x, t) + p'_L(x, t) + p'_Q(x, t) \quad (8)$$

Farassat's formulation 1A, a nonconvective form of the FWH for general subsonic source regions, is preferred for acoustic analysis (Farassat 1983). The thickness surface term (monopole) $p'_T(x, t)$ generated by the displacement of fluid that passed the body is defined as follows.

$$p'_T(x, t) = \frac{1}{4\pi} \left(\int_{(f=0)} \left[\frac{\rho_0 \left(\dot{U}_n + U \frac{\dot{n}}{r} \right)}{r(1-M_r)^2} \right]_{\text{ret}} dS + \int_{(f=0)} \left[\frac{\rho_0 U_n \left[r \dot{M}_r + a_0 (M_r - M^2) \right]}{r^2 (1-M_r)^3} \right]_{\text{ret}} dS \right) \quad (9)$$

The loading surface term (dipole) $p'_L(x, t)$ depends on the variation of the force distribution on the body surface. It is given as follows.

$$p'_L(x, t) = \frac{1}{4\pi} \left(\frac{1}{a_0} \int_{(f=0)} \left[\frac{\dot{L}_r}{r(1-M_r)^2} \right]_{\text{ret}} dS + \int_{(f=0)} \left[\frac{L_r - L_M}{r^2 (1-M_r)^2} \right]_{\text{ret}} dS + \int_{(f=0)} \left[\frac{L_r \left[r \dot{M}_r + a_0 (M_r - M^2) \right]}{r^2 (1-M_r)^3} \right]_{\text{ret}} dS \right) \quad (10)$$

The quadrupole noise $p'_Q(x, t)$ accounts for turbulence mixing as a volumetric source, and it is given as

$$p'_Q(x, t) = \frac{1}{4\pi} \left(\left(\frac{1}{c} \right) \left(\frac{\partial^2}{\partial t^2} \right) \int_{-\infty}^t \left[\int_{f>0} \frac{T_{rr}}{r} d\Omega \right] d\tau + \left(\frac{\partial}{\partial t} \right) \int_{-\infty}^t \left[\int_{f>0} \frac{3T_{rr} - T_{ii}}{r^2} d\Omega \right] d\tau + c \int_{f>0} \left[\int_{f>0} \frac{3T_{rr} - T_{ii}}{r^3} d\Omega \right] d\tau \right) \quad (11)$$

where U represents the fluid velocity; L_i and T_{rr} are the blade load vector and the Lighthill stress tensor, respectively; ρ_0 is the far-field density; r is the distance from a source point to the observer; and M_r is the Mach number of the source toward the observer. The subscript *ret* indicates retarded time, and a dot above a variable defines the derivative with respect to source time for that variable. Moreover, $f=0$ denotes a mathematical surface to embed the exterior flow problem ($f>0$) in an unbounded space. The quadrupole source is assessed as a “collapsing-sphere” formulation (Eqs. 11 and 12) in which the space derivatives are transformed into time derivatives (Brentner and Farassat 1998).

$$p'_Q(x, t) = \frac{1}{4\pi} \left(\int_{f>0} \left[\frac{K_1}{c^2 r} + \frac{K_2}{cr^2} + \frac{K_3}{r^3} \right]_{\text{ret}} dV \right) \quad (12)$$

3 Experimental Setup and Procedure

Hydro-acoustic experiments were performed in a silent circulation tunnel at the Ata Nutku Ship Model Testing Laboratory, Istanbul Technical University. A circular cylinder diameter and span length of $D = 0.02$ m and $L = 30.0D$, respectively, were used in the experiments. The size of the circulation channel was $L = 6$ m, $W = 1.75$ m, and $H = 1$ m. The cylinder spanned the entire test section, with the size of $W = 1.35$ m and $H = 0.85$ m. The measurements were performed for the Reynolds number of 2.25×10^4 .

The acoustic measurements were recorded using a Bruel & Kjaer (B&K) 8104 hydrophone fixed to the streamlined strut. A specific mechanism was designed to locate the hydrophone in different underwater positions. The form of the mechanism was modeled based on a design used in the flow noise measurements in the literature to generate minimum noise levels (Felli 2006; Pereira et al. 2016). The cylinder was also installed in the test section by taking preventative measures for the silent underwater medium. The hydrophone was located at a distance of 5 diameters downward and 25 diameters behind the cylinder center for the recordings of the noise measurements. The hydrophone position was determined such that the depth-dependent effects near the water surface and interference effects close to the bottom surface were avoided

(de Jong et al. 2011). The data obtained from the hydrophone were analyzed by the B&K 3560-B-049 analyzer during the postprocessing phase. The measurement accuracy was ± 1 dB for the hydro-acoustic experiments. The schematic diagram of the experimental rig used to perform acoustic experiments is shown in Figure 1.

The background noise consisted of the mechanical noise from the pump and other mechanisms in the cavitation tunnel. The noise tests showed that the noise levels generated by the flow around the circular cylinder were distinguishable from the background noise. Figure 2 displays the test section with the circular cylinder and the hydrophone mechanism.

4 Numerical Procedure

The realizable two-layer k-epsilon, SST k-omega, IDDES, and LES models were used to model the turbulent flow structures around the circular cylinder in the fluid dynamics analyses. Farassat's 1A integral formulation of the FWH equation with quadrupole sources was implemented for the acoustic simulations. The numerical analyses were performed for three Reynolds numbers: 2.25×10^4 , 4.5×10^4 , and 9.0×10^4 . All flow and acoustic simulations were performed through the computer software STAR-CCM+ v12.04.011 double precision by Siemens.

The computational domain was $29.2D$ (diameter) long in the streamwise x -direction. The inlet and exit boundaries were placed at $8.6D$ and $20.6D$ from the cylinder axis, respectively. The positions of the top and bottom boundaries were at $10.3D$ from the cylinder axis (Lehmkuhl et al. 2014). The spanwise length was determined as $2.5D$ to resolve any spanwise flow structure of a large length scale (Patankar and Spalding 1972). Using a fine mesh structure is necessary to obtain time-accurate data on the near-field flow, since the data are utilized as input for the determination of the noise sources in the FWH equation. It is also important for the accurate prediction of the boundary layer and to satisfy the requirements for turbulence models. Therefore, the grid independence study was

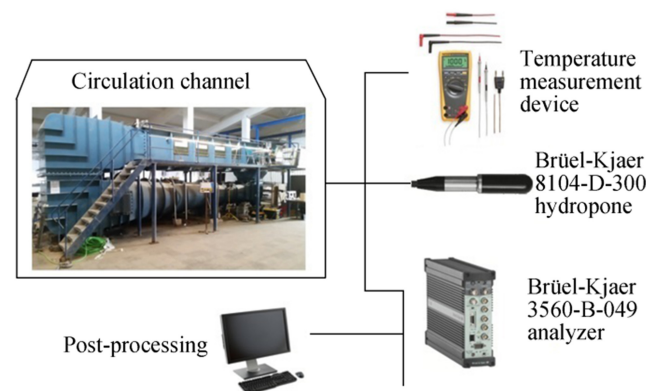


Figure 1 Schematic diagram of experimental rig

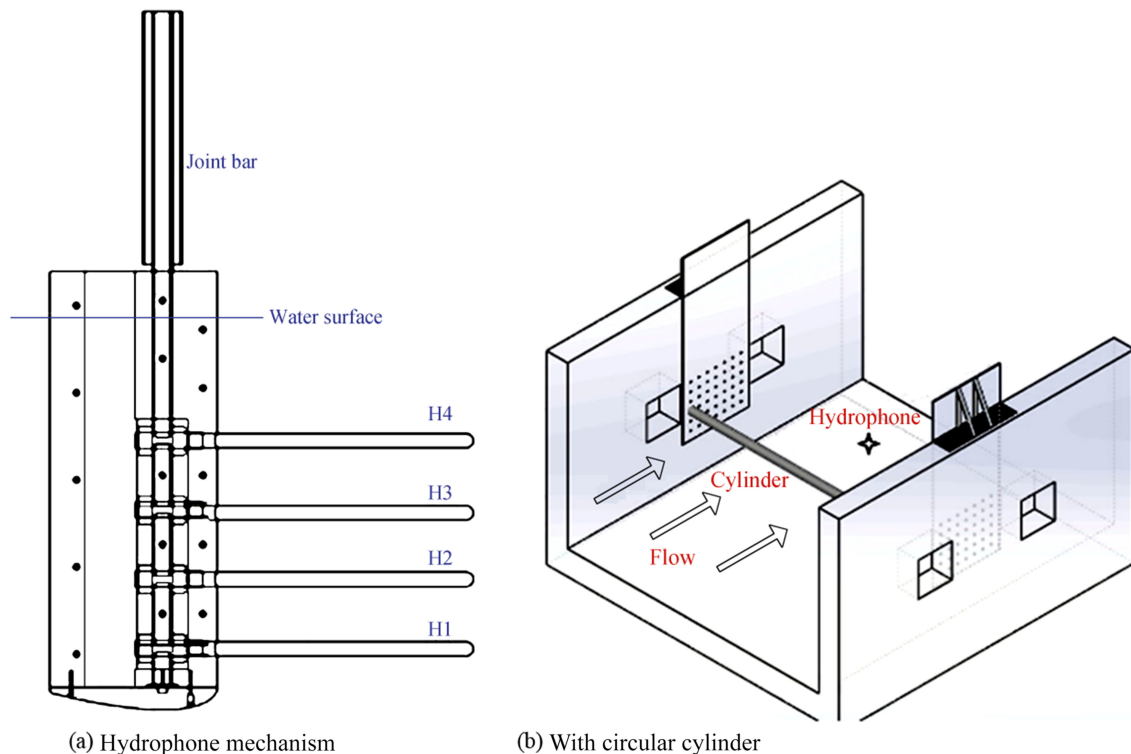


Figure 2 Test section of experimental rig

performed to provide the best suitable mesh structures required for the flow analyses. The block-structured hexahedral grids with a total of 5.4, 10.3, and 14.2 million cells were used for RANS, DES, and LES models, respectively. The grid refinement was performed around the cylinder wall and within the cylinder wake, especially. A spatial mesh resolution of $\Delta y^+ \approx 1$ was used by considering the grid resolution requirements of the near-wall region. Figure 3 shows the details of the mesh structure around the cylinder surface and within the computational domain.

The time step of $\Delta t = 2 \times 10^{-5}$ s and 20 substeps were adopted to ensure a Courant–Friedrichs–Lewy number of less than 1 in all cells of the domain, so that the calculation converges within each time step. For each numerical simulation, approximately 18 000 time steps were considered. It took nearly 3 weeks to complete each numerical case using all existing processor cores in a DELL Precision T7810 workstation with two Intel Xeon E5-2640v4 processors and 160-GB DDR4 RAM.

A spanwise periodicity condition was specified for the two lateral boundaries. A constant freestream pressure and a constant freestream velocity without any turbulence velocity components were applied for the inlet and exit boundaries, respectively. All the numerical calculations of the continuity and momentum were performed using the finite volume method. This method transforms the mathematical model into a system of algebraic equations by discretizing the governing equations in space and time. The algebraic multigrid methods were used to solve the resulting linear equations. The SIMPLE algorithm was employed for

pressure velocity coupling for different Reynolds numbers (Travin et al. 2000). Bounded-central differencing (BCD) was used as the discretization scheme for RANS and LES models, while hybrid-BCD was utilized for the DES model. The hybrid-BCD scheme blends second-order upwind and BCD. The convective terms are discretized by the second-order upwind scheme, while the second-order time-discretization together with an implicit scheme is used for the time integration.

The effects of the temperature on acoustic properties were investigated within the range of 10–50 °C for the water and air media. The effects of the salinity between 10 and 70 g/kg were evaluated for the water medium. Four receiver points (R1, R2, R3, and R4) used for the acoustic analysis were positioned perpendicular to the flow direction and downward of the cylinder at distances of $5D$, $10D$, $15D$, and $20D$ away from the cylinder center. Unsteady pressure fluctuations data obtained from receivers were transformed from the time domain to the frequency domain using the fast-Fourier transform functions. The reference sound pressure was considered as 1.0×10^{-6} Pa for the water and 2.0×10^{-5} Pa for the air. The Hann (Hanning) function was used as the window function.

5 Results of Computational Fluid Dynamics Modeling and Comparisons with Experiments

The accuracy of the predictions of acoustic spectra directly depends on the precision of the dynamic analysis to simulate

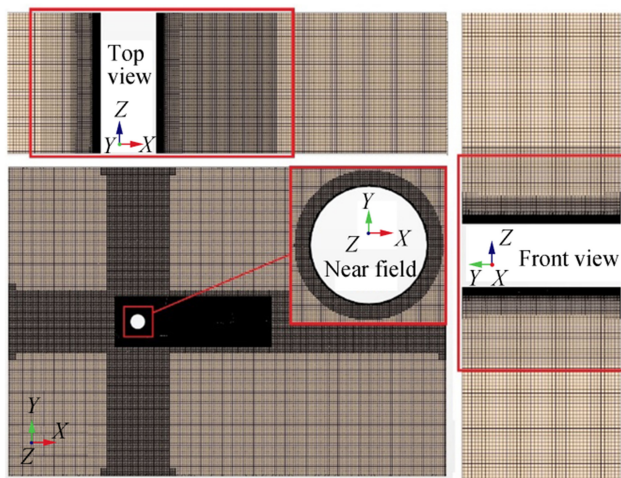


Figure 3 Various views of computational grid

the turbulent flow structures. The turbulence model capabilities of capturing the noise-generating eddies over a wide range of length scales have importance for the determination of the acoustic characteristics over a bluff body. The hybrid methods, which combine RANS, DES, or LES turbulence models with the FWH equation, were investigated by comparison with the experimental data. The benchmark parameters such as the mean drag coefficient ($\overline{C_D}$), angle of flow separation (θ_s), shedding frequency (St), pressure coefficient (C_p), friction coefficient (C_f), wall Y^+ function, and the root mean square values of the fluctuating drag and lift coefficients (C'_D , C'_L) were used to evaluate the flow analysis accuracy.

Table 1 compares the hydrodynamic results obtained from k-epsilon ($k-\epsilon$), k-omega ($k-\omega$), DES, and LES turbulence models at a Reynolds number of 1.28×10^5 with the corresponding experimental data. The values of $C'_{D_{rms}}$ and $C'_{L_{rms}}$ were quite sensitive to the choice of the turbulent model. The data of $C'_{D_{rms}}$ and $C'_{L_{rms}}$ obtained from the realizable k-epsilon significantly differed from the literature results

(West and Apelt 1993; Cantwell and Coles 1983), whereas DES and LES matched well with the earlier findings. Each turbulence model presented reasonable results in terms of the mean drag coefficient, within the experimental data range.

The azimuthal distributions of C_p and the dimensionless form of C_f over the cylinder surface are presented for all turbulence models in Figure 4. From Figure 4 and Table 1, the flow separation angles (θ_s) determined by the DES and LES models show satisfactory agreement with those reported by Travin et al. (2000), with a 2.0%–6.0% difference.

The vortex shedding is the main sound-generation mechanism related to the pressure fluctuations on the cylinder surface. The shedding frequencies obtained by DES and LES, which corresponds to the Strouhal number $St = 0.19$ and 0.18 , respectively, appear to be well supported by the reported values in the literature, with a 0.5%–5.0% difference (Norberg 2003; Bearman 1969; Park 2012).

Figure 5 shows the three-dimensional flow structures based on the Q-Criterion in the cylinder wake for the Reynolds number of 1.28×10^5 . The laminar region in the front of the cylinder and the turbulent oscillating wake in the rear can be seen in detail for each turbulence model. As shown in the figure, the LES and DES turbulence models captured the vortices behind the cylinder better than the RANS models.

Figure 6 compares the mean pressure and skin-friction coefficients along the cylinder surface obtained by DES with the experimental data at a Reynolds number of 9.0×10^4 (Cantwell and Coles 1983; Achenbach 1968). The surface pressure distribution obtained by the DES mostly matched well with the measured values for the region around the cylinder surface. The flow separation angle was determined by DES as 85° , which agrees with the experimental data of 82° . The error percentages between the DES simulations and experiments (Cantwell and Coles 1983; Achenbach 1968) are presented in Table 2. In general, the pressure and mean dimensionless skin-friction coefficients were well predicted by

Table 1 Comparisons of flow quantities of θ_s , St , $C'_{L_{rms}}$, $\overline{C_D}$, and $C'_{D_{rms}}$ for $Re = 1.28 \times 10^5$

Flow quantities	k- ϵ	k- ω	DES	LES	Exp. data
θ_s ($^\circ$)	116	110	105	101	99 (Travin et al. 2000)
St	0.26	0.21	0.19	0.18	0.179–0.19 (Norberg 2003; Bearman 1969; Park 2012)
$C'_{L_{rms}}$	0.34	0.66	0.42	0.49	0.49–0.58 (Norberg 2003; Szepessy 1992; West and Apelt 1993)
$\overline{C_D}$	0.96	1.27	1.01	0.95	0.49–0.58 (Norberg 2003; Szepessy 1992; West and Apelt 1993)
$C'_{D_{rms}}$	0.03	0.12	0.13	0.15	0.9–1.4 (Cantwell and Coles 1983)
Y^+	0.48	0.49	0.45	0.44	0.13–0.18 (West and Apelt 1993)

DES; however, they were overpredicted after the flow separation. At the separation angle of 82° , the error percentages for the pressure and skin-friction coefficients were 11.58% and 5.71%, respectively.

The details of the flow path behind the cylinder for the Reynolds number of 9.0×10^4 are presented in Figure 7 using streamlines. The separation points and vortices in the streamline plot are shown in this plot.

The accuracy of the turbulence models was evaluated by comparing the benchmark parameters with the literature findings. The DES and LES models enabled a reliable prediction of turbulent fluctuations for fluid dynamics analyses and gave better agreement than RANS models. The DES model was also evaluated to determine flow parameters for aerodynamic simulations, and it showed reasonable agreement with the corresponding experimental data.

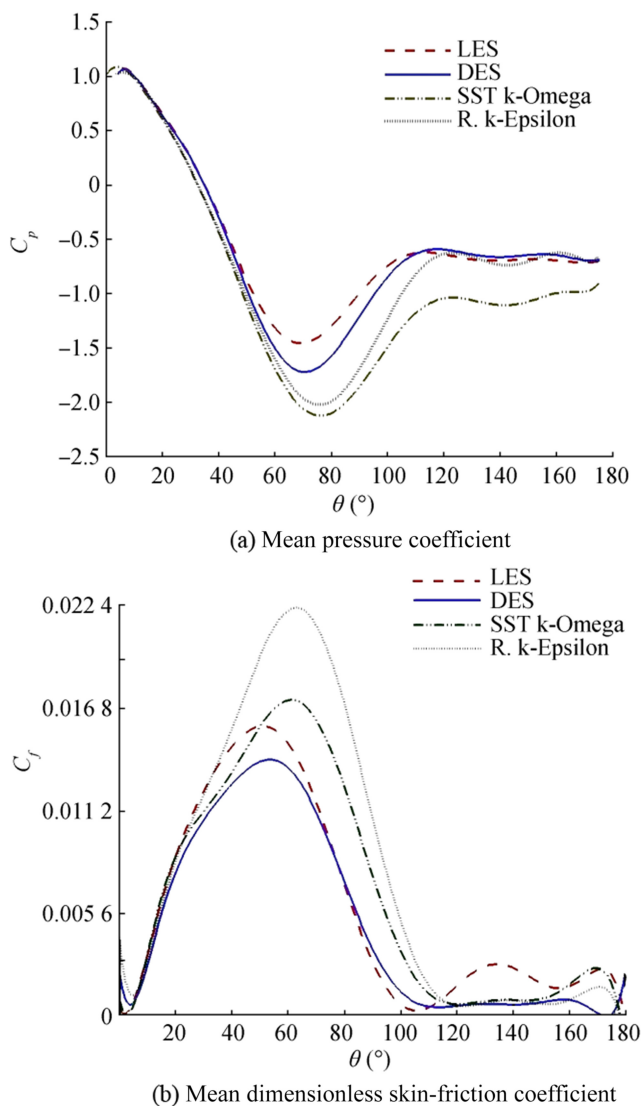


Figure 4 Azimuthal distributions of pressure and skin-friction coefficients for $Re = 1.28 \times 10^5$ (a) Mean pressure coefficient (b) Mean dimensionless skin-friction coefficient

6 Results of Acoustic Analyses and Comparisons with Experiments

In this study, the hybrid methods of k-omega with FWH, DES with FWH, and LES with FWH were investigated to evaluate their prediction capacities of hydro-acoustic characteristics by comparing their results with the measurements. Farassat's 1A formulation of the FWH equation with quadrupole sources was used to determine acoustic characteristics in the analyses. Hydro-acoustic analyses and measurements were performed for the Reynolds number of 2.25×10^4 . The hydrophone was located at a distance of 5 diameters downward and 25 diameters behind the cylinder center for the analyses and measurements. The background noise levels were measured with unsteady flow through the empty test section for the Reynolds number used in the experiments. The frequencies of the anechoic part of the test chamber were below 600 Hz, and the noise levels generated by the flow around the circular cylinder were distinguishable from the background noise.

The acoustic results were evaluated in terms of the SPL in the decibel scale (dB). The SPL (dB) can be defined as follows:

$$\text{SPL} = 20\log(P_e/P_{\text{ref}}) \quad (13)$$

where P_e denotes the effective sound pressure and P_{ref} is defined as the reference pressure, which was taken as $1 \mu\text{Pa}$ in water and $20 \mu\text{Pa}$ in air. The OASPL was obtained by summing the contributions of all acoustic spectrum results, as given in the following expression:

$$\text{OASPL} = 20\log\sqrt{\sum_i 10^{(\text{SPL}_i/20)^2}} \quad (14)$$

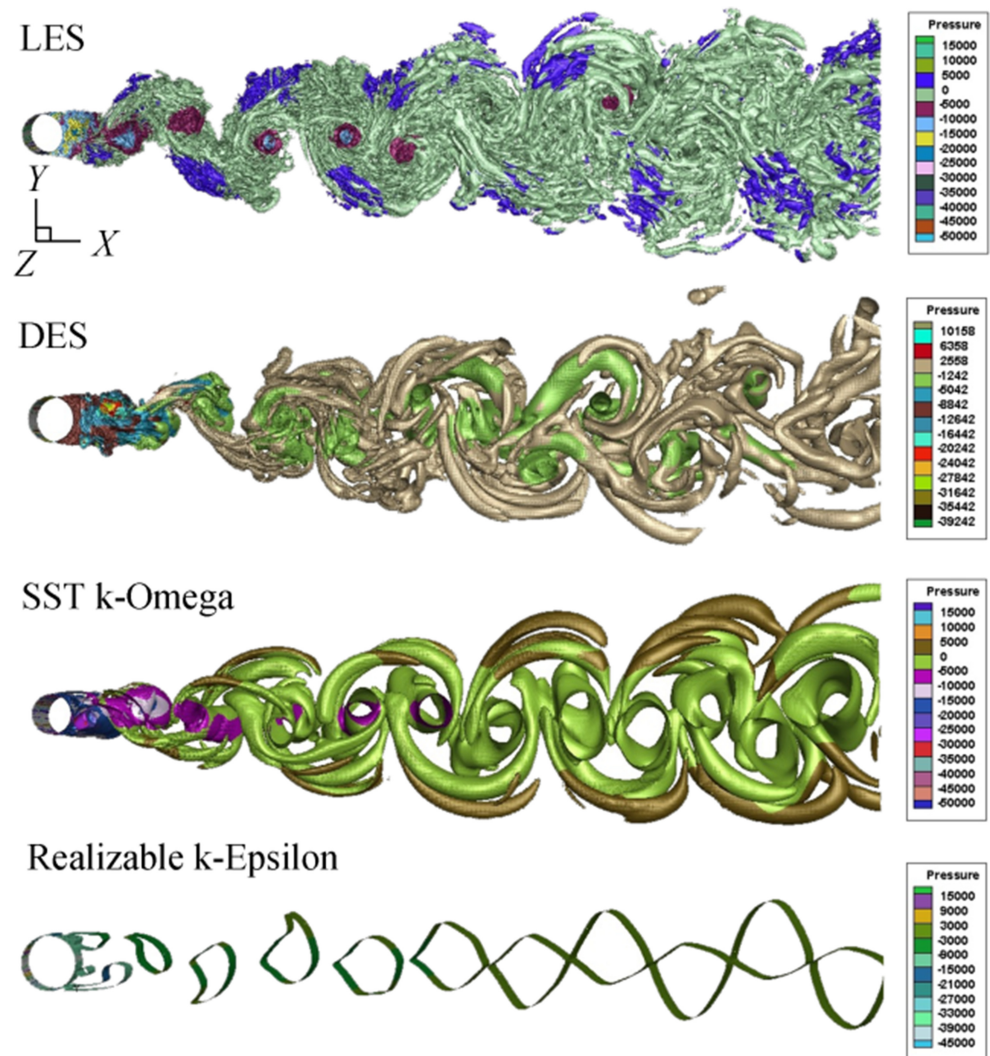
The spanwise dimension of the model used in numerical simulations was $2.5D$, which was $1/12$ of the experimental model. Therefore, it is necessary to utilize a correction method to consider the effect of the longer span length used in the measurements. The Kato correction method (Kato et al. 2007) was utilized to consider the additional sound level generated due to the longer span length of the cylinder. The correction formula is as follows:

$$\begin{aligned} L_C \leq L_S & \quad \Delta\text{SPL}_{\text{corr}} = 10\log(L/L_S) \\ L_S \leq L_C \leq L & \quad \Delta\text{SPL}_{\text{corr}} = 20\log(L_C/L_S) + 10\log(L/L_C) \\ L \leq L_C & \quad \Delta\text{SPL}_{\text{corr}} = 20\log(L/L_S) \end{aligned} \quad (15)$$

where L , L_S , and L_C are the span length, simulation length, and correlation length, respectively. According to the study by Norberg (2003), the correlation length was $L_C \approx 9D$ for the Reynolds number used in this acoustic analysis. This corresponds to an increase by 16 dB for the predicted SPLs.

Figure 8 presents the SPL spectra of the cylinder based on the frequency obtained by hybrid methods

Figure 5 Flow structure view behind smooth cylinder for $Re = 1.28 \times 10^5$ (colored by pressure magnitude)



and hydro-acoustic measurements. The comparisons with the measured spectra showed that the hybrid methods of DES-FWH and LES-FWH performed excellently to resolve the harmonics in the low-frequency region. These models well predicted the SPL_T , as the values agreed well with the measurement results, while k-omega with the FWH model significantly

Table 2 Error percentages between DES results and experimental data by Cantwell and Coles (1983) and Achenbach (1968)

Pressure coefficient		Skin-friction coefficient	
θ (°)	Error (%)	θ (°)	Error (%)
25	5.15	28	2.95
44	2.04	47	4.87
82	11.58	82	5.71
120	15.05	134	28.14

overpredicted the SPL_T . Especially, the slight difference of over 600 Hz was due to the effect of the background noise.

Table 3 presents the main characteristics of the SPL spectrum, namely, the main peak frequency (denoted by f_T); the SPL at this frequency, that is, the maximum SPL (SPL_T in dB); and the OASPL in dB. The DES-FWH and LES-FWH models provided the best predictions in terms of the maximum SPL, within about 2 dB of the spectra obtained directly from the hydrophone signals in measurements. Regarding the OASPL, the predictions of these models accurately matched with experimental values, while the LES-FWH model had a slightly better agreement than the DES-FWH for the main peak frequency. The omega-FWH model had difficulty in capturing both the maximum SPLs and broadband noise levels but exhibited reasonable performance for the vortex shedding frequency.

Regarding the fluid dynamics and acoustic analyses, the DES-FWH and LES-FWH models best agreed with the

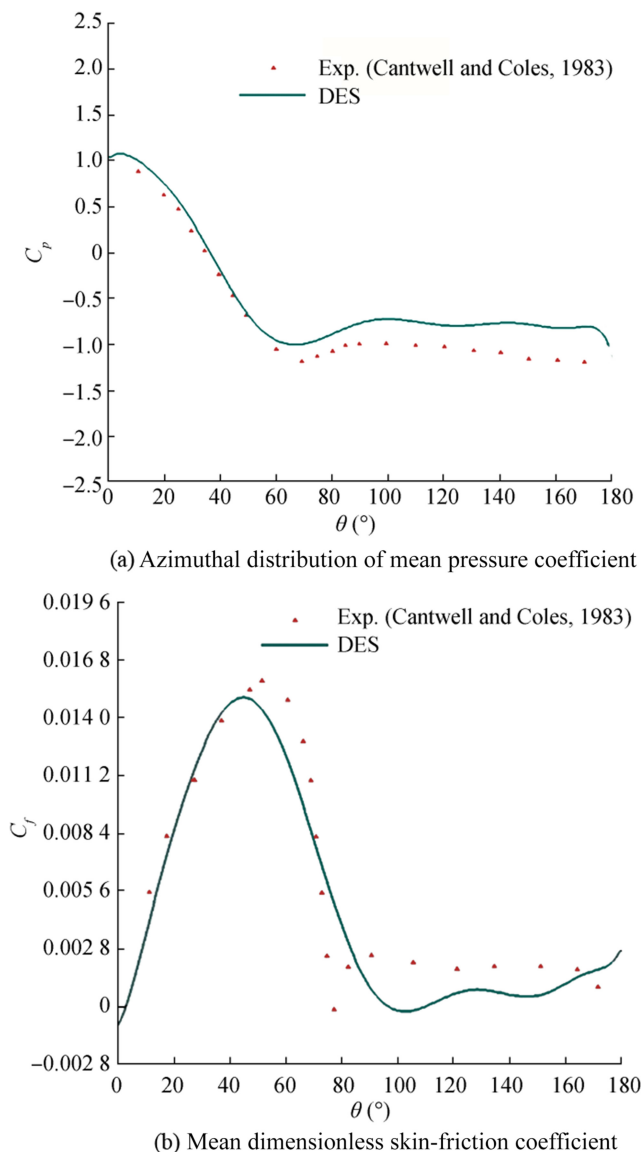


Figure 6 Azimuthal distribution of mean pressure coefficient and mean dimensionless skin-friction coefficient for $Re = 9.0 \times 10^4$. (a) Azimuthal distribution of mean pressure coefficient (b) Mean dimensionless skin-friction coefficient

experimental data. As for the computational costs, the DES-

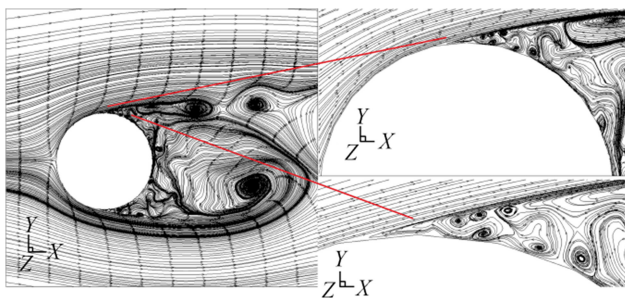


Figure 7 Streamline plot of the flow past circular cylinder for $Re = 9.0 \times 10^4$

FWH model was more suitable for performing the acoustic analysis to investigate the effects of temperature, salinity ratio, and fluid type on the acoustic characteristics of the circular cylinder.

7 Results of the Effects of Temperature, Salinity, and Fluid Type on Acoustic Characteristics

The acoustic characteristics of the circular cylinder were numerically obtained by considering the effects of temperature, salinity ratio, and fluid type. The hybrid method DES-FWH was employed for the numerical simulations due to its capability for predicting the turbulent flow structures and the acoustic spectrum. The aero- and hydro-acoustic simulations were performed for the Reynolds numbers of 2.25×10^4 , 4.5×10^4 , and 9.0×10^4 at four different receiver points. The effects of temperature, salinity ratio, and fluid type on the main acoustic characteristics were evaluated by considering the main acoustic characteristics, such as broadband noise, main peak frequency (f_T), SPL_T , and OASPL. The range of temperature and salinity ratios was determined by considering the properties of the oceans and seas and their usage in engineering applications. The effects of the temperature on the acoustic properties were investigated within the range of 10–50 °C for the water and air media. The effects of the salinity between 10 and 70 g/kg were evaluated for the water medium. In addition, the acoustic characteristics obtained for water and air media were compared in terms of the frequency spectrum.

The acoustic spectra obtained for different water temperatures are displayed in Figure 9 for the Reynolds number of 9.0×10^4 . The spectral shape significantly changed with the increase in temperature. As the water temperature increased from 10 °C to 50 °C, the main peak frequency, at which the maximum SPLs were observed, decreased from about 68–22 Hz. The broadband noise ($f > 1$ kHz) decreased with the increase in the water temperature. The maximum decrease of about 15 dB in the broadband noise occurred between the temperature values 30 °C and 50 °C.

Figure 10a presents the variations of the SPL_T and the OASPL with the water temperature at Reynolds numbers of 2.25×10^4 , 4.5×10^4 , and 9.0×10^4 . The dotted and solid lines represent the SPL_T and OASPL, respectively. In general, the OASPL and SPL_T values decreased with the increase in the water temperature. For example, when the temperature increased from 10 °C to 50 °C, the OASPL decreased from about 152.1 to 135.7 dB for the Reynolds number of 9.0×10^4 , and the SPL_T from about 150.2 to 134.5 dB (Figure 10a). The variations of the OASPL and SPL_T values with the receiver distance are presented in Figure 10b. When the receiver distance increased fourfold, from R1 to R4, the OASPL and SPL_T values decreased by the maximum amount, about 23.5 and

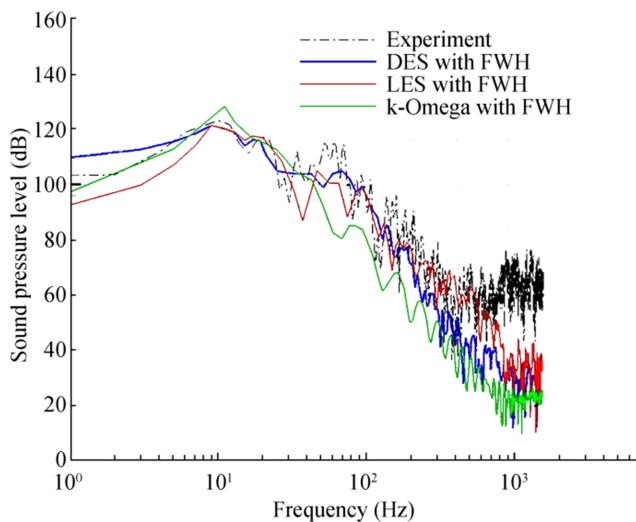


Figure 8 Comparisons of SPL spectra obtained from hybrid methods and experiments

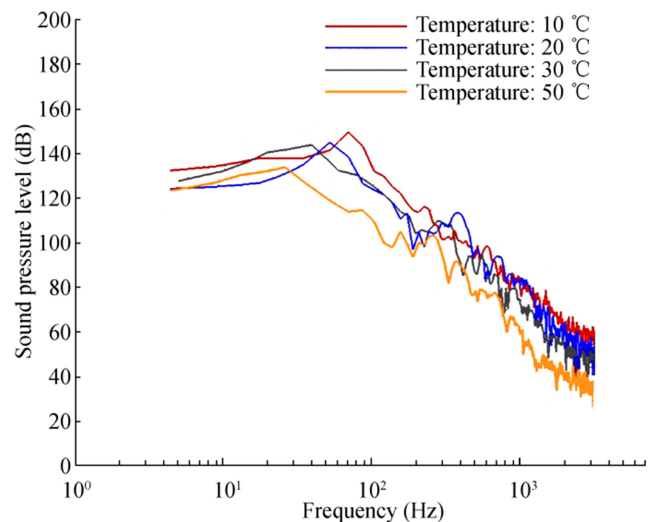


Figure 9 Comparisons of SPL spectra obtained for various water temperatures at receiver R1

23.6 dB, respectively. As shown in Figure 10b, the maximum decrease occurred at the air temperature of 50 °C.

The temperature effect on the viscosity of liquids is different from that for gases. The intermolecular forces of attraction are greater, and the molecules are less loosely packed in liquids than in gases. When the liquid is gaining heat, the energy level of molecules and the distance between them increase, which causes the intermolecular forces of attraction to weaken, and thus, the viscosity decreases. Viscous shear stress is the main source of the dipole noise (Hu et al. 2002; Shariff and Wang 2005). The wall shear is equal to the viscous shear at the wall for smooth walls (see, Eq. (16)), and the turbulence is almost totally damped. Therefore, molecular viscosity becomes the most important factor. Increasing the temperature from 10 °C to 50 °C resulted in a 57.7% reduction in the water viscosity. The noise level reduction at all Reynolds numbers was due to the viscosity reduction, which weakened the dipole source strength. Hence, a 1.3% decrease in the density with the increase in water temperature had a slight diminishing impact on the quadrupole source strength (Cocking 1974; Hoch and Duponchel 1973).

Table 3 Comparisons of computed acoustic data with experimental data

Sound parameters	Exp.	LES-FWH	DES-FWH	Omega-FWH
f_T (Hz)	10	9	9	12
SPL _T (dB)	123.3	121.5	121.4	128.4
OASPL (dB)	125.9	125.2	125.0	129.9

$$\tau = \mu \frac{d\bar{u}}{dy} = \tau_w \quad (16)$$

Figure 11 presents the variations of acoustic spectra with the air temperature for the Reynolds number of 9.0×10^4 . The increase in the fluid temperature affected the main peak frequency, f_T ; the effect in the air medium was different from that in the water medium. When the air temperature increased from 10 °C to 50 °C, the main peak frequency increased from about 664 to 968 Hz. The broadband noise ($f > 1$ kHz) increased with an increase in the air temperature. There is a maximum increase of about 17 dB between the temperature values of 30 °C and 50 °C.

An increase in the temperature of a gas causes an increase in the molecular interchange and further intensifies the chaotic molecular motion. Consequently, the gas viscosity increases. Therefore, the heating of the air medium caused an increase in its viscosity, unlike for the water medium. The studies by Hu et al. (2002) and Shariff and Wang (2005) indicate that viscous shear stress can be a true source of sound and treats as a dipole with its dominance over quadrupole sources at low Mach numbers ($M < 1$). In the current study, the air viscosity increased by about 10.4% with the temperature increase from 10 °C to 50 °C. This strengthened the dipole sources. A decrease of about 15.5% in density within the same temperature range undermines the quadrupole sources. However, the total noise levels increased with an increase in air temperature, as the dipole sources were more dominant than quadrupole sources for the Reynolds numbers considered.

The SPL_T and OASPL obtained for different air temperatures are shown in Figure 12a. The OASPL and SPL_T values increased with an increase in the air temperature. For instance,

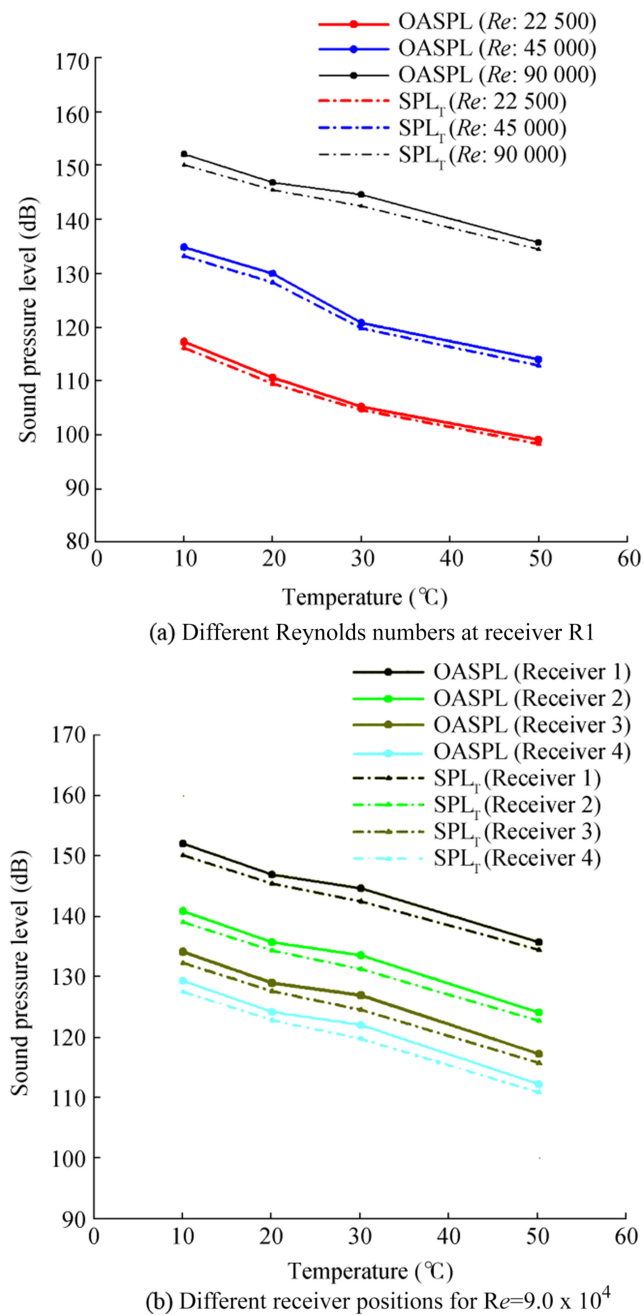


Figure 10 Variations of OASPL and SPL_T with the water temperature (a) Different Reynolds numbers at receiver R1 (b) Different receiver positions for $Re = 9.0 \times 10^4$

the OASPL increased from about 101.2 to 110.8 dB, and the SPL_T from about 91.4 to 104.2 dB between the air temperature values of 10 °C to 50 °C for the Reynolds number of 9.0×10^4 . When the receiver distance was quadrupled, the OASPL value decreased by the maximum amount, about 12.8 dB, for the air temperature of 20 °C, and the SPL_T value also decreased by the maximum amount, about 13.0 dB, for the air temperature of 50 °C (Figure 12b).

Figure 13 shows acoustic spectra for the salinity values of 10, 30, 50, and 70 g/kg. The main peak frequency was

nearly independent of the water salinity. The broadband noise ($f > 1$ kHz) increased with an increase in water salinity. It had a maximum increase of about 8 dB when the salinity increased from 50 to 70 g/kg.

The effects of salinity on the fluid viscosity can be explained by two mechanisms. First, each ion added to the water can be treated as an independent particle carrying momentum within the fluid. Second, the ionic interaction generates a certain resistance to the shear directly related to the fluid viscosity (Kwak et al. 2005). When the water salinity increased from 10 to 70 g/kg, the viscosity increased by about 14.4%. As a result, the dipole source strength increased. Also, the density increased with salinity by about 3.9%, and this increased the quadrupole source strength.

The changes in the acoustic characteristics of OASPL and SPL_T with the water salinity are illustrated in Figure 14a. The OASPL and SPL_T values increased with the water salinity. At the Reynolds number of 9.0×10^4 , the OASPL value increased from about 141.0 to 151.7 dB and the SPL_T from about 137.6 to 150.5 dB. When the receiver distance increased fourfold, from R1 to R4, the OASPL decreased by the maximum amount, about 23.0 dB, for the water salinity of 10 g/kg; the SPL_T also decreased by the maximum amount, about 22.7 dB, for the water salinity of 30 g/kg (Figure 14b).

Figure 15 compares the acoustic spectra obtained for the water and air media. The spectral shape alters significantly by the fluid type. The noise levels obtained from the water and air media showed similar characteristics for the broadband noise at high frequencies ($f > 1$ kHz). However, the acoustic characteristics for both media were completely different at low frequencies ($f < 1$ kHz).

The main acoustic characteristics, that is, the main peak frequency (f_T), SPL_T , and OASPL for water and air media, are presented in Table 4. The main peak frequency for the air medium was higher than that for the water medium. The main

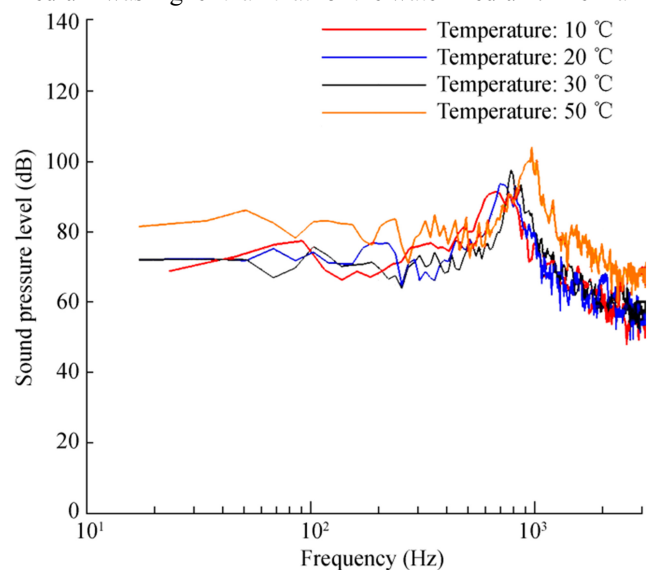


Figure 11 Comparisons of SPL spectra obtained for various air temperatures at receiver R1

peak frequency was 52 Hz for the water medium and 696 Hz for the air medium at the Reynolds number of 9.0×10^4 . The differences in the SPL_T and OASPL values between water and air media were considerably high. For instance, the OASPL values were 146.9 and 103 dB for the water and air media at the Reynolds number of 9.0×10^4 , respectively.

This difference in the SPL_T and OASPL values between the two media was due to the difference in the fluid properties of the air and water media. For example, the water viscosity was about 57 times the air viscosity, and the water density was

about 841 times the air density for the temperature of 20 °C. Particularly, the difference in the viscosity was the dominant factor affecting the dipole sources. The other factor was the difference in density, which contributes to the noise levels by strengthening the quadrupole sources.

8 Conclusions

This study numerically investigated the effects of temperature, salinity, and fluid type on the acoustic characteristics of turbulent flow around a circular cylinder. Hydro- and aero-acoustic analyses were conducted to evaluate these parameters for a circular cylinder and at Reynolds numbers of 2.25×10^4 , 4.5×10^4 , and 9.0×10^4 . The capabilities of the hybrid models (RANS-FWH, DES-FWH, and LES-FWH) to predict the turbulent flow structures and acoustic characteristics were examined by comparing the results with the experimental data. The hybrid method DES-FWH was chosen as an appropriate method for the analyses by considering the simulation cost and the accuracy of the results with the experimental findings. Hydro-acoustic measurements were also performed at the Reynolds number of 2.25×10^4 in a silent circulation channel. The temperature values within the range of 10–50 °C were examined for water and air media. The salinity values between 10 and 70 g/kg were evaluated for the water medium. The acoustic spectra obtained for the water and air media were compared for various Reynolds numbers.

The important findings of the investigation are as follows:

- 1) Increasing the water temperature from 10 °C to 50 °C resulted in about 57.7% and 1.3% decrease in water viscosity and density, respectively. Therefore, the temperature increase for water had diminishing effects on the

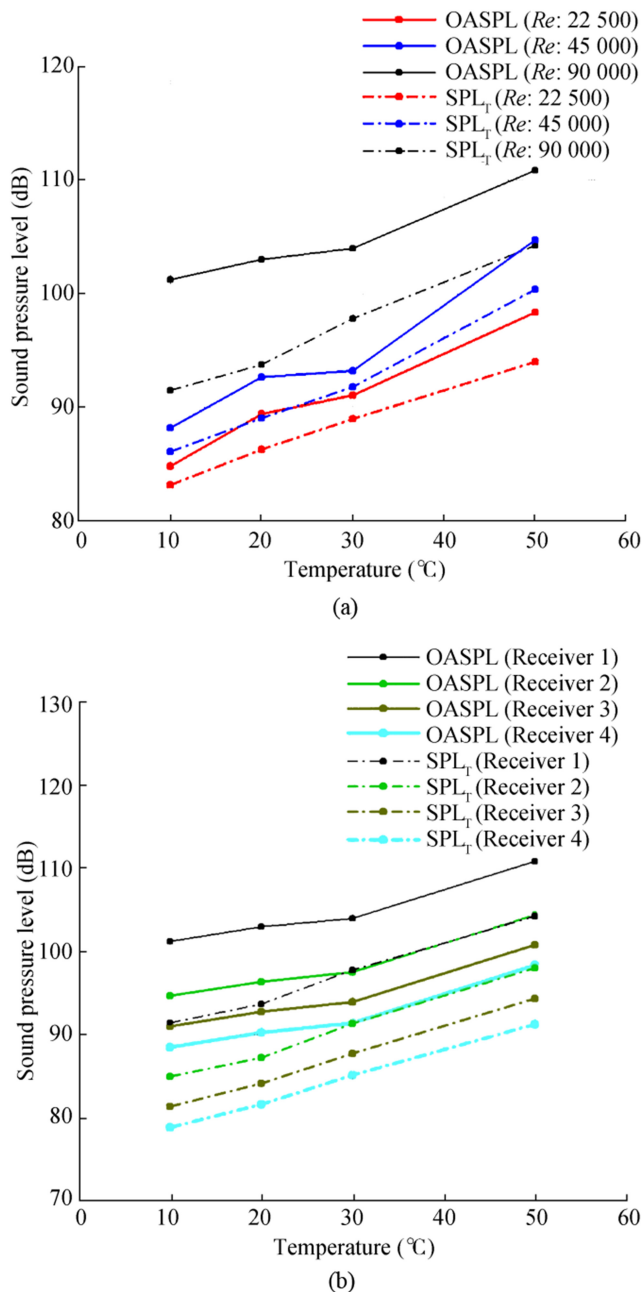


Figure 12 Variations of OASPL and SPL_T with air temperature (a) Different Reynolds numbers at the receiver R1 (b) Different receiver of $Re=9.0 \times 10^4$

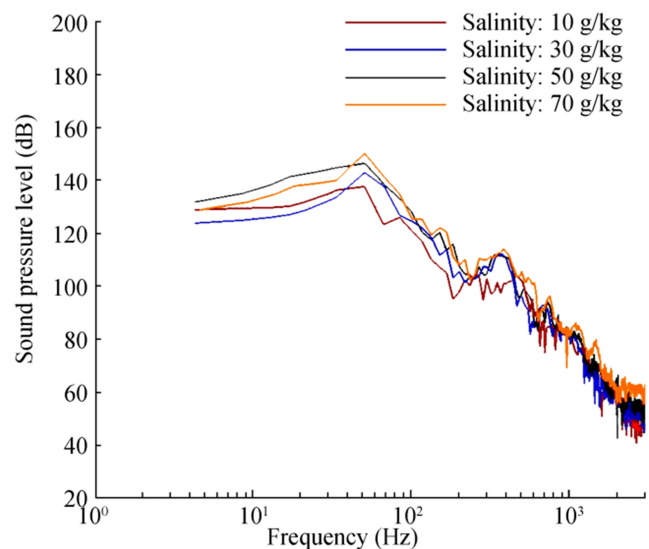
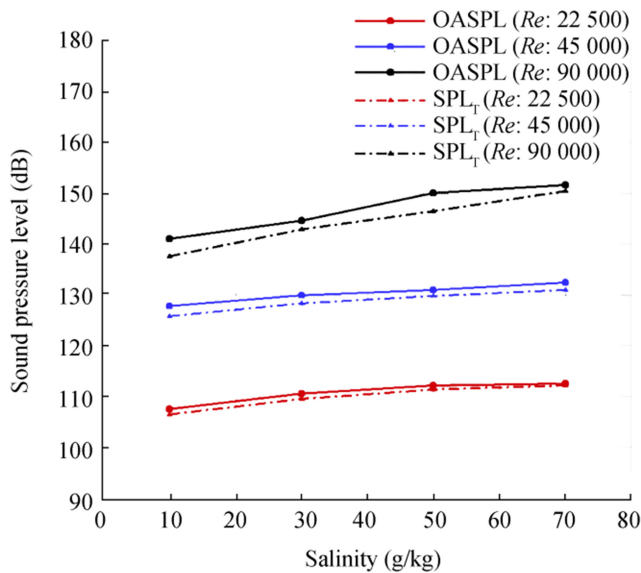
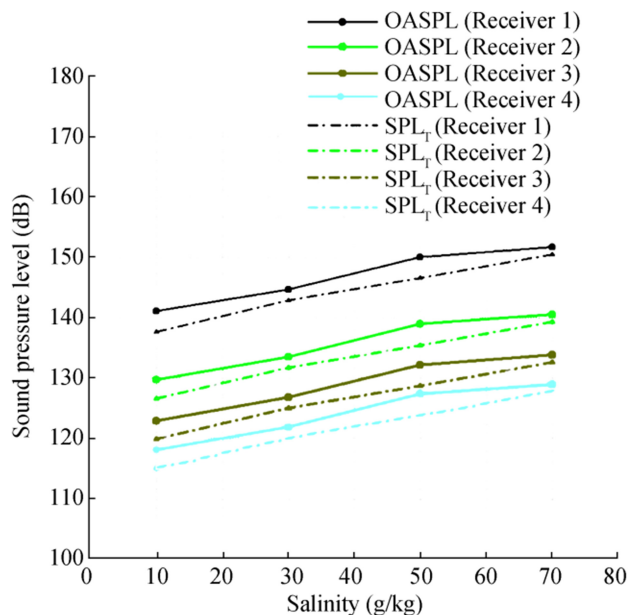


Figure 13 Comparisons of SPL spectra obtained for various salinity ratios (receiver: R1)

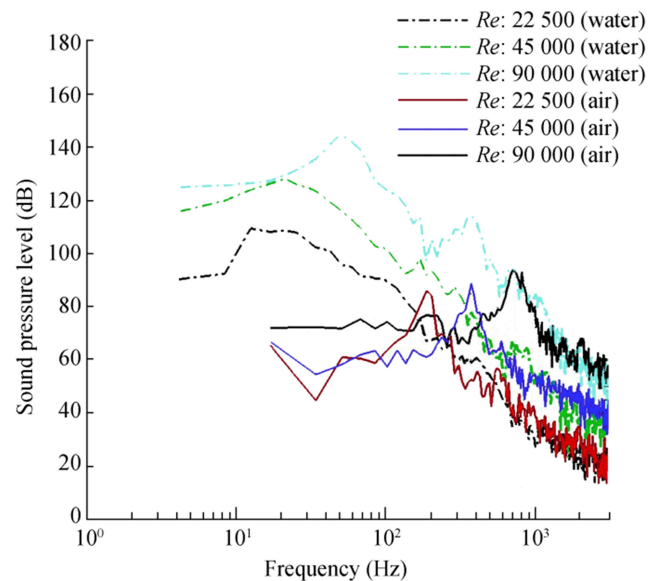


(a) Salinity ratio (receiver: R1)

(b) Receiver position ($Re=9.0 \times 10^4$)**Figure 14** Variation of OASPL and SPL_T . (a) Salinity ratio (receiver: R1) (b) Receiver position ($Re=9.0 \times 10^4$)

dipole and quadrupole source strength. When the water temperature was increased from 10 °C to 50 °C, the OASPL decreased from about 152.1 to 135.7 dB, and the SPL_T from about 150.2 to 134.5 dB for the Reynolds number of 9.0×10^4 .

- 2) An increase in the air temperature from 10 °C to 50 °C led to about 10.4% increase in the air viscosity and 15.5% decrease in the air density. This had strengthening effects on the dipole sources but weakening effects on the quadrupole sources. As the dipole sources were more dominant than the quadrupole sources for the Reynolds numbers considered, the total noise levels increased with an

**Figure 15** Comparisons of acoustic spectra obtained from water and air media (temperature: 20 °C, receiver: R1)**Table 4** f_T , SPL_T , and OASPL for water and air media (temperature: 20 °C, receiver: R1)

Fluid type	Sound parameters	$Re=2.25 \times 10^4$	$Re=4.5 \times 10^4$	$Re=9.0 \times 10^4$
Water	f_T	12	22	52
	SPL_T	109.5	128.3	145.5
	OASPL	110.6	130.0	146.9
Air	f_T	186	374	696
	SPL_T	86.2	89.0	93.7
	OASPL	89.4	92.6	103

increase in the air temperature. The OASPL increased from about 101.2 to 110.8 dB and the SPL_T from about 91.4 dB to 104.2 dB between the air temperature values of 10 °C and 50 °C for the Reynolds number of 9.0×10^4 .

- 3) With increase in the salinity from 1×10^{-5} to 7×10^{-5} , the water viscosity and density increased by about 14.4% and 3.9%, respectively. This led to an increase in the strength of dipole and quadrupole sources. When the salinity increased from 10 to 70 g/kg, the OASPL value increased from about 141.0 to 151.7 dB for the Reynolds number of 9.0×10^4 and the SPL_T from about 137.6 to 150.5 dB.
- 4) The shape of the acoustic spectrum significantly depends on the fluid type. The acoustic characteristics were completely different for the water and air media at low frequencies ($f < 1$ kHz). The main peak frequency for the air medium was higher than that for the water medium. The differences in the SPL_T and OASPL values between water and air media were considerably high. For instance, the OASPL values for the water and air media were 146.9

and 103 dB, respectively, at the temperature of 20 °C for the Reynolds number of 9.0×10^4 . This was due to the difference in the fluid properties of the media.

- 5) The effects of the increase in the fluid temperature on the main peak frequency f_T differed based on the fluid type. An increase in the temperature caused a reduction in the main peak frequency for the water medium, while it led to an increase in the main peak frequency for the air medium. Interestingly, the main peak frequency was nearly independent of the water salinity.
- 6) The broadband noise ($f > 1$ kHz) decreased with an increase in the water temperature but increased with an increase in the air temperature. Also, an increase in the salinity led to an increase in the broadband noise. The noise levels obtained from the water and air media showed similar characteristics for the broadband noise at high frequencies ($f > 1$ kHz).

Overall, this study presents valuable information on the effects of temperature, salinity, and fluid type on the acoustic characteristics of turbulent flow around a circular cylinder. It further clarifies the complex nature and structure of aero- and hydro-acoustics.

References

- Achenbach E (1968) Distribution of local pressure and skin friction around a circular cylinder in cross-flow up to $Re = 5 \times 10^6$. *J Fluid Mech* 34(4):625–639. <https://doi.org/10.1017/S0022112068002120>
- Akyildiz IF, Pompili D, Melodia T (2005) Underwater acoustic sensor networks: research challenges. *Ad Hoc Netw* 3(3):257–279. <https://doi.org/10.1016/j.adhoc.2005.01.004>
- Awan KM, Shah PA, Iqbal K, Gillani S, Ahmad W, Nam Y (2019) Underwater wireless sensor networks: a review of recent issues and challenges. *Wirel Commun Mob Comput* 2019(3):1–20. <https://doi.org/10.1155/2019/6470359>
- Bagheri MR, Hamid M, Mohammad SS, Omar Y (2017) Analysis of noise behaviour for marine propellers under cavitating and non-cavitating conditions. *Ships Offshore Struct* 12(1):1–8. <https://doi.org/10.1080/17445302.2015.1099224>
- Bearman PW (1969) On vortex shedding from a circular cylinder in the critical Reynolds number regime. *J Fluid Mech* 37(3):577–585
- Benderskiy LA, Lyubimov DA (2014) Investigation of flow parameters and noise of subsonic and supersonic jets using RANS/ILES high-resolution method. 29th Congress of the Int. Counc. Of the Aeronautical Sciences, St. Petersburg, Russia, p 0373
- Bodony DJ, Lele SK (2005) On using large-eddy simulation for the prediction of noise from cold and heated turbulent jets. *Phys Fluids* 17(8):085103. <https://doi.org/10.1063/1.2001689>
- Bogey C, Marsden O (2013) Numerical investigation of temperature effects on properties of subsonic turbulent jets. 19th AIAA/CEAS Aeroacoustics Conference, Berlin, Germany, p 2140. <https://doi.org/10.2514/6.2013-2140>
- Bosschers J, Lafeber FH, de Boer J, Bosman R, Bouvy A (2013) Underwater radiated noise measurements with a silent towing carriage in the depressurized wave basin. AMT'13, Gdańsk, Poland
- Boussinesq J (1877) Essai sur la theorie des eaux courantes. *Memories presents par divers savants a l'Academic des Science de l'Institut de France*:1–680
- Brentner KS, Farassat F (1998) Analytical comparison of the acoustic analogy and kirchoff formulation for moving surfaces. *AIAA J* 36(8):1379–1386. <https://doi.org/10.2514/2.558>
- Brentner KS, Farassat F (2003) Modelling aerodynamically generated sound of helicopter rotors. *Prog Aerosp Sci* 39(2-3):83–120. <https://doi.org/10.1260/1475-472X.13.7-8.533>
- Bridges J (2006) Effect of heat on space-time correlations in jets. 12th AIAA/CEAS Aeroacoustics Conference, Cambridge, Massachusetts, p 2534. <https://doi.org/10.2514/6.2006-2534>
- Bulut S, Ergin S (2018) An investigation on the effects of various flow parameters on the underwater flow noise. *NAV* 2018, Trieste, Italy, pp 133–140. <https://doi.org/10.3233/978-1-61499-870-9-133>
- Cantwell B, Coles D (1983) An experimental study of entrainment and transport in the turbulent near wake of a circular cylinder. *J Fluid Mech* 136:321–374. <https://doi.org/10.1017/S0022112083002189>
- Choi WS, Choi YS, Hong SY, Song JH, Kwon HW, Seol HS, Jung CM (2016) Turbulence-induced noise of a submerged cylinder using a permeable FW-H method. *Int J Naval Arc Ocean Eng* 8(3):235–242. <https://doi.org/10.1016/j.ijnaoe.2016.03.002>
- Choi YS, Choi WS, Hong SY, Song JH, Kwon HW, Seol HS, Jung CM (2017) Development of formulation Q1As method for quadrupole noise prediction around a submerged cylinder. *Int J Naval Arc Ocean Eng* 9(5):484–491. <https://doi.org/10.1016/j.ijnaoe.2017.02.002>
- Cianferra M, Armenio V, Ianniello S (2018) Hydro-acoustic noise from different geometries. *Int J Heat Fluid Flow* 70:348–362. <https://doi.org/10.1016/j.ijheatfluidflow.2017.12.005>
- Cianferra M, Ianniello S, Armenio V (2019) Assessment of methodologies for the solution of the Ffowcs Williams and Hawkings equation using LES of incompressible single-phase flow around a finite-size square cylinder. *J Sound Vib* 453:1–24. <https://doi.org/10.1016/j.jsv.2019.04.001>
- Cocking BJ (1974) The Effect of Temperature on Subsonic Jet Noise. National Gas Turbine Establishment (NGTE), Report No. R331.
- Cox JS, Rumsey CL, Brentner SK, Younis BA (1997) Computation of Sound Generated by Viscous Flow Over a Circular Cylinder. NASA Technical Report No. TM 110339.
- Curle N (1955) The influence of solid boundaries upon aerodynamic sound. *Proc R Soc Lond A* 231(1187):505–514. <https://doi.org/10.1098/rspa.1955.0191>
- Dawi AH, Akkermans RAD (2018) Direct and integral noise computation of two square cylinders in tandem arrangement. *J Sound Vib* 436:138–154. <https://doi.org/10.1063/1.5063642>
- de Jong C.A.F., Ainslie M.A., Blacquièrre G., 2011. Standard for measurement and monitoring of underwater noise, Part II: procedures for measuring underwater noise in connection with offshore wind farm licensing. TNO Report No. TNO-DV 2011 C251.
- Farassat F (2007) Derivation of formulations 1 and 1A of Farassat. NASA Technical Report No. TM-2007-214853.
- Farassat F, Succi GP (1983) The prediction of helicopter discrete frequency noise. *Vertica* 7(4):309–320
- Felli M (2006). Noise measurements techniques and hydrodynamic aspects related to cavitation noise. Report No. TNE5-CT-2006-031316.
- Ganta N, Bikash M, Bhumkar YG (2019) Analysis of sound generation by flow past a circular cylinder performing rotary oscillations using direct simulation approach. *Phys Fluids* 31(2):026104. <https://doi.org/10.1063/1.5063642>

- Germano M, Piomelli U, Moin P, Cabot WH (1991) A dynamic subgrid-scale eddy viscosity model. *Phys Fluids* 3(7):1760–1765. <https://doi.org/10.1063/1.857955>
- Hoch RG, Duponchel JP (1973) Studies of the influence of density on jet noise. *J Sound Vib* 28(4):649–668. [https://doi.org/10.1016/S0022-460X\(73\)80141-5](https://doi.org/10.1016/S0022-460X(73)80141-5)
- Hu ZH, Morfey CL, Sandham ND (2002) Aeroacoustics of wall-bounded turbulent flows. *AIAA J* 40(3):465–473. <https://doi.org/10.2514/2.1697>
- Hutcheson FV, Brooks TF (2012) Noise radiation from single and multiple rod configurations. *Int J Aeroacoustics* 11(3–4):291–334. <https://doi.org/10.1260/1475-472X.11.3-4.291>
- Ianniello S (2016) The Ffowcs Williams-Hawkings equation for hydroacoustic analysis of rotating blades. Part 1. The rot pole. *J Fluid Mech* 797:345–388. <https://doi.org/10.1017/jfm.2016.263>
- Ianniello S, De Bernardis E (2015) Farassat's formulations in marine propeller hydroacoustics. *Int J Aeroacoustics* 14(1–2):87–103. <https://doi.org/10.1260/1475-472X.14.1-2.87>
- Imran AZM, Hossen MM, Islam MT (2017) Capacity optimization of underwater acoustic communication system. In: 3rd Int. Conf. Electr. Eng. and Inf. Comm. Tech. ICEEICT, pp 8–12. <https://doi.org/10.1109/CEEICT.2016.7873087>
- Inoue O, Hatakeyama N (2002) Sound generation by a two-dimensional circular cylinder in a uniform flow. *J Fluid Mech* 471:285–314. <https://doi.org/10.1017/S0022112002002124>
- Jones WP, Launder BE (1972) The prediction of laminarization with a two-equation model of turbulence. *Int J Heat Mass Transf* 15(2):301–314. [https://doi.org/10.1016/0017-9310\(72\)90076-2](https://doi.org/10.1016/0017-9310(72)90076-2)
- Kato C, Yamade Y, Wang H, Guo Y, Miyazawa M, Takaishi T, Yoshimura S, Takano Y (2007) Numerical prediction of sound generated from flows with a low Mach number. *Comput Fluids* 36(1):53–68. <https://doi.org/10.1016/j.compfluid.2005.07.006>
- Kuo CW, McLaughlin DK, Morris PJ, Viswanathan K (2015) Effects of jet temperature on broadband shock-associated noise. *AIAA J* 53(6):1515–1530. <https://doi.org/10.2514/1.J053442>
- Kwak HT, Zhang G, Chen S, Atlas B (2005) The effects of salt type and salinity on formation water viscosity and NMR responses, vol 21. Proceedings of the international symposium of the Society of Core Analysts, Toronto, Canada, pp 1–13
- Lehmkuhl O, Rodríguez I, Borrell R, Chiva J, Oliva A (2014) Unsteady forces on a circular cylinder at critical Reynolds numbers. *Phys Fluids* 26(12):125110. <https://doi.org/10.1063/1.4904415>
- Lighthill MJ (1952) On sound generated aerodynamically, I. General theory. *Proc R Soc A* 211(1107):564–587. <https://doi.org/10.1098/rspa.1952.0060>
- Lilly DK (1992) A proposed modification of the Germano subgrid-scale closure method. *Phys Fluids A Fluid Dyn* 4(3):633–635. <https://doi.org/10.1063/1.858280>
- Liu N, Wang S, Guo T, Li X, Yu Z (2011) Experimental research on the double-peak characteristic of underwater radiated noise in the near field on top of a submarine. *J Mar Sci Appl* 10(2):233–239. <https://doi.org/10.1007/s11804-011-1049-2>
- Lockard DP, Khorrami MR, Choudhari MM, Hutcheson FV, Brooks TF, Stead DJ (2007) Tandem cylinder noise predictions, vol 3450. 13th AIAA/CEAS Aeroacoustics Conf, Rome, Italy, pp 1–26. <https://doi.org/10.2514/6.2007-3450>
- Mahato B, Ganta N, Bhumkar YG (2018) Direct simulation of sound generation by a two-dimensional flow past a wedge. *Phys Fluids* 30(9):096101. <https://doi.org/10.1063/1.5039953>
- Menter FR (1993) Zonal two equation $k-\omega$ turbulence models for aerodynamic flows, AIAA Paper, pp 93–2906. <https://doi.org/10.2514/6.1993-2906>
- Norberg C (2003) Fluctuating lift on a circular cylinder: review and new measurements. *J Fluids Struct* 17(1):57–96. [https://doi.org/10.1016/S0889-9746\(02\)00099-3](https://doi.org/10.1016/S0889-9746(02)00099-3)
- Park IC (2012) 2-Dimensional Simulation of Flow-Induced Noise around Circular Cylinder. Thesis and Dissertations, Chungnam University
- Patankar SV, Spalding DB (1972) A calculation procedure for heat, mass and momentum transfer in three-dimensional parabolic flows. *Int J Heat Mass Transf* 15(10):1787–1806. [https://doi.org/10.1016/0017-9310\(72\)90054-3](https://doi.org/10.1016/0017-9310(72)90054-3)
- Pereira FA, Felice F, Salvatore F (2016) Propeller cavitation in non-uniform flow and correlation with the near pressure field. *J Mar Sci Eng* 4(4):70. <https://doi.org/10.3390/jmse4040070>
- Proudman I (1952) The generation of noise by isotropic turbulence. *Proc R Soc Lond* 214(1116):119–132. <https://doi.org/10.1098/rspa.1952.0154>
- Revell JD, Prydz RA, Hays AP (1978) Experimental study of aerodynamic noise vs drag relationships for circular cylinders. *AIAA J* 16(9):889–897. <https://doi.org/10.2514/3.60982>
- Sehgal A, Tumar I, Schönwälder J (2009) Variability of available capacity due to the effects of depth and temperature in the underwater acoustic communication channel. Proceedings of the OCEANS IEEE, Bremen, Germany, pp 1–6. <https://doi.org/10.1109/OCEANSE.2009.5278268>
- Sendra S, Lloret J, Jimenez JM, Parra L (2016) Underwater acoustic modems. *IEEE Sensors J* 16(11):4063–4071. <https://doi.org/10.1109/JSEN.2015.2434890>
- Shariff K, Wang M (2005) A numerical experiment to determine whether surface shear-stress fluctuations are a true sound source. *Phys Fluids* 17(107105):1–11. <https://doi.org/10.1063/1.2112747>
- Spalart PR, Jou WH, Strelets M, Allmaras SR (1997) Comments on the feasibility of LES for wings, and on a hybrid RANS/LES approach. Proceedings of First AFOSR Int. Conf. on DNS/LES, Ruston, LA, pp 137–148
- Szepessy S (1992) Aspect ratio and end plate effects on vortex shedding from a circular cylinder. *J Fluid Mech* 234:191–217. <https://doi.org/10.1017/S0022112092000752>
- Tanna HK, Dean PD, Fisher MJ (1975) The influence of temperature on shock-free supersonic jet noise. *J Sound Vib* 39(4):429–460. [https://doi.org/10.1016/S0022-460X\(75\)80026-5](https://doi.org/10.1016/S0022-460X(75)80026-5)
- Testa C, Ianniello S, Salvatore FA (2018) Ffowcs Williams and Hawkings formulation for hydroacoustic analysis of propeller sheet cavitation. *J Sound Vib* 413:421–441. <https://doi.org/10.1016/j.jsv.2017.10.004>
- Travin A, Shur M, Strelets M, Spalart P (2000) Detached-eddy simulations past a circular cylinder. *Flow Turbul Combust* 63(1):293–313. <https://doi.org/10.1023/A:1009901401183>
- West GS, Apelt CJ (1993) Measurements of fluctuating pressure and forces on a circular cylinder in the Reynolds number range 10^4 to 2.5×10^5 . *J Fluids Struct* 7(3):227–244. <https://doi.org/10.1006/jfls.1993.1014>
- Williams JE, Hawkings DL (1969) Sound generation by turbulence and surfaces in arbitrary motion. *Philos Trans R Soc Lond A* 264(1151):321–342. <https://doi.org/10.1098/rsta.1969.0031>
- Zaibi G, Nasri N, Kachouri A, Samet M (2009) Survey of temperature variation effect on underwater acoustic wireless transmission. *ICGST-CNIR J* 9(2):1–6
- Zhang C, Sanjose M, Moreau S (2019) Aeolian noise of a cylinder in the critical regime. *J Acoust Soc Am* 146(2):1404–1415. <https://doi.org/10.1121/1.5122185>